Wetting of Heterogeneous Nanopatterned Inorganic Surfaces

Mikael Järn,[†] Felix J. Brieler,[†] Monica Kuemmel,[‡] David Grosso,[‡] and Mika Lindén*,[†]

Department of Physical Chemistry, Åbo Akademi University, Porthansgatan 3-5, FI-20500 Turku, Finland, and Chimie de la Matière Condensée, UMR UPMC-CNRS 7574, 4 place Jussieu, 75252 Paris 05, France

Received October 4, 2007. Revised Manuscript Received November 22, 2007

The wetting of heterogeneous nanopatterned surfaces composed of an ultrathin TiO_2 layer homogeneously perforated by nanocraters through which the surface of the substrate (SiO_2 or Au) is accessible has been investigated by water contact angle measurements. The evaporation-induced (surfactant) self-assembly (EISA) conditions used to prepare such TiO_2 nanoperforated films allowed the crater dimension to be adjusted to 11 and 30 nm. The hydrophilic−hydrophobic contrast of the films was varied through selective functionalization of the TiO_2 portion of the film with Zonyl functions. Detailed structural characterization of the nanoperforated layers using AFM, SEM, ellipsometry, and electrochemistry allowed the results to be quantitatively evaluated on the basis of existing models for wetting of heterogeneous and rough surfaces. Three different types of wetting were observed, depending on the hydrophilic−hydrophobic contrast and the volume and means of deposition of the water droplet. For hydrophilic nanoperforated layers, full wetting of the films as a result of 3D capillary wetting was observed, regardless of the absolute value of the contact angle of the substrate. When 2 μL water droplets were used, hydrophobically functionalized films with hydrophilic craters showed advancing contact angles exceeding 120°, regardless of the hydrophilicity of the substrate. In this case, the contact angles could be described within a few degrees by the Cassie−Baxter formalism, which assumes that a composite solid−vapor surface exists below the droplet. However, when droplets with larger volumes were dropped onto the surface, the contact angles of the composite films decreased and could be fairly well described by a combination of the Cassie and Wenzel equations, which assume full contact of the water droplet with the film. The large contact-angle hysteresis observed suggests that an intermediate state between the Cassie−Baxter and Cassie−Wenzel models possibly exists. Also, the geometry of the nanopatterned surfaces contributes to a large hysteresis, since a long, continuous contact line can form.

Introduction

Micro- and nanostructured surfaces have recently attracted a great deal of interest because of prospects for their wide range of applications, including microelectronics,[1] microfluidics,[2,3] nanotribology, and sensing,[4,5] and work on these surfaces has recently been reviewed.[6] Patterning can, for example, be used to modulate the properties of the surface between conducting and insulating areas in modified electrodes, create patterned surfaces with tunable surface energy for localized attachment of living cells,[7] adjust the molecular affinity and recognition for sensing, or influence the 3D growth of subsequently deposited layers. The wetting properties, especially in connection with water condensation from the gas phase, are immensely important for applications of nanopatterned films in sensing and microelectronics, as the condensation of water changes the conductivity of the films and could thus lead to short-circuiting or erroneous readout signals.

Many studies of the wetting of rough surfaces having different geometries have been performed, but most of them employed model surfaces with heterogeneity length scales of micrometers or several hundred nanometers in at least one dimension and films with thicknesses typically exceeding hundreds of nanometers.[8–16] This is surely connected to experimental difficulties in preparing homogeneously patterned surfaces in which the level of heterogeneity is in the nanometer range. Lithographic techniques, templating using

* To whom correspondence should be addressed: mlinden@abo.fi.
[†] Åbo Akademi University.
[‡] UMR UPMC-CNRS 7574.

(1) Hieda, M.; Garcia, R.; Dixon, M.; Allara, D.; Chan, M. H. W. *Appl. Phys. Lett.* **2004**, *84*, 628.
(2) Kusumaatmaja, H.; Yeomans, J. M. *Langmuir* **2007**, *23*, 956.
(3) Handique, K.; Burke, D. T.; Mastrangelo, C. H.; Burns, M. A. *Anal. Chem.* **2000**, *72*, 4100.
(4) Lehmann, U.; Hadjidj, S.; Parashar, V. K.; Vandevyver, C.; Rida, A.; Gijs, M. A. M. *Sens. Actuators, B* **2006**, *117*, 457.
(5) Lee, S. H.; Cho, S. I.; Lee, C. S.; Kim, B. G.; Kim, Y. K. *Sens. Actuators, B* **2005**, *110*, 164.
(6) Feng, X.; Jiang, L. *Adv. Mater.* **2006**, *18*, 3063.
(7) Wang, Y.; Sims, C. E.; Marc, P.; Bachman, M.; Li, G. P.; Allbritton, N. L. *Langmuir* **2006**, *22*, 8257.
(8) Lau, K. K. S.; Bico, J.; Teo, K. B. K.; Chhowalla, M.; Amaratunga, G. A. J.; Milne, W. I.; McKinley, G. H.; Gleason, K. K. *Nano Lett.* **2003**, *3*, 1701.
(9) Burton, Z.; Bhushan, B. *Nano Lett.* **2005**, *5*, 1607.
(10) Abdelsalam, M. E.; Bartlett, P. N.; Kelf, T.; Baumberg, J. *Langmuir* **2005**, *21*, 1753.
(11) Suh, K. Y.; Jon, S. *Langmuir* **2005**, *21*, 6836.
(12) Martines, E.; Seunarine, K.; Morgan, H.; Gadegaard, N.; Wilkinson, C. D. W.; Riehle, M. O. *Nano Lett.* **2005**, *5*, 2097.
(13) Shibuichi, S.; Onda, T.; Satoh, N.; Tsuji, K. *J. Phys. Chem.* **1996**, *100*, 19512.
(14) Bico, J.; Marzolin, C.; Quere, D. *Europhys. Lett.* **1999**, *47*, 220.
(15) Öner, D.; McCarthy, T. J. *Langmuir* **2000**, *16*, 7777.
(16) Yoshimitsu, Z.; Nakajima, A.; Watanabe, T.; Hashimito, K. *Langmuir* **2002**, *18*, 5818.

10.1021/cm702870r CCC: $40.75 © 2008 American Chemical Society
Published on Web 01/05/2008

latex spheres,[17] layer-by-layer assembly of surface-functionalized inorganic particles,[18] or microphase separation approaches[19,20] have been used to fabricate such patterned surfaces, and normally, micrometer-level heterogeneity has been achieved. Alternatively, nanometer-level patterning has been attempted using electrochemical deposition or self-assembled monolayer[21] or silanization approaches that were prematurely discontinued in order to yield incomplete surface coverage,[22,23] thus resulting in patterned surfaces. However, such approaches often suffered from inhomogeneous deposition, making it difficult to experimentally determine fractional areas and roughness values with the high accuracy needed for quantitative theoretical analysis. Creation of nanopatterned surfaces with edge resolutions better than 10 nm can be accomplished by a nanografting process, which combines the displacement of selected resist molecules by an atomic force microscope tip and the adsorption of new adsorbate.[24] However, methods such as this are tedious and do not easily lend themselves to patterning of macroscopic surfaces. Self-organizing polymer films have been studied, but these films may suffer from chemical instability toward the liquid probe solution.[25] Recently, the wetting behavior of truly nanopatterned surfaces was reported,[26] in which Au and SiO_x films were prepared by ion-milling. This is one of the few wetting studies of nanopatterned, well-structured surfaces that has been reported. We recently reported another means of preparing nanopatterned surfaces:[27] continuous networks of well-perforated thin layers of TiO_2 on SiO_2 wafers were successfully prepared using a simple evaporation-induced (surfactant) self-assembly (EISA)-driven approach, where the craters were aligned exclusively in the direction perpendicular to the substrate. This represents an important step toward utilizing the full potential of porous oxide films in applications related to microelectronics and sensing, among others. The crater diameters can be tuned between 10 and 50 nm, depending on the size of the surfactant used as the template. An important property of such composite films is that selective surface functionalization is easy to achieve because organophosphates bind selectively to the TiO_2 portion of the surface. Full accessibility of the silica substrate after functionalization of the TiO_2 was evidenced by subsequent selective surface functionalization of the SiO_2 substrate by silanes. Successful selective functionalization was verified by XPS measurements.[27] Importantly, a wide range of experimental techniques can be used to characterize these films, including atomic force microscopy (AFM) for analysis of local nanometer-scale structure (crater diameter, wall thickness, film thickness), scanning electron microscopy (SEM) for crater diameter and wall thickness, and ellipsometry for porosity and film thickness. Thus, these layers are ideal for use as model surfaces for studies of wetting of nanopatterned surfaces.

Two common models are normally used to describe the wetting of rough or patterned surfaces. In the Wenzel model,[28] the liquid is assumed to completely wet the grooves of a single-component rough surface. The apparent contact angle θ_A is then given by

$$\cos \theta_A = r \cos \theta_Y \quad (1)$$

where r is the ratio of the actual and projected surface areas of the sample and θ_Y is the Young contact angle. The equation thus states that a rough hydrophilic surface ($\theta_Y < 90°$) should be more hydrophilic and a rough hydrophobic surface ($\theta_Y > 90°$) more hydrophobic than a flat surface with the same chemical composition.

In the case of a flat, chemically heterogeneous surface, the wetting is typically described by applying the Cassie equation.[29] For a two-component system with an ideally flat surface, the wetting is described by

$$\cos \theta_A = f_1 \cos \theta_1 + f_2 \cos \theta_2 \quad (2)$$

where f_1 and f_2 are the area fractions of materials 1 and 2, respectively, and θ_1 and θ_2 are the contact angles on pure materials 1 and 2, respectively. Assuming that air is entrapped in the voids of a rough surface ($\theta_2 = 180°$) and using the fact that $f_1 + f_2 = 1$ enables the Cassie equation to be written as

$$\cos \theta_A = -1 + f_1(\cos \theta_1 + 1) \quad (3)$$

Equation 3 is generally called the Cassie−Baxter equation.[30] Several authors have shown that a liquid droplet on a rough hydrophobic surface can be in either a Wenzel or a Cassie−Baxter state, depending on how the droplet is formed. Bico et al.[14] reported that a liquid droplet could be transferred from a Cassie−Baxter state to a Wenzel state when physically pressed. Patankar and co-workers[31,32] showed that the contact angle of a water droplet that was gently deposited on a rough hydrophobic surface could be modeled using the Cassie−Baxter equation. When the droplet was dropped onto the same surface from some height, the water contact angle was considerably smaller. These studies suggest that a transition between two energy states can occur and that the activation energy of the transition can be fairly low. The geometric parameters of the surface determine the global minimum-energy state.

Despite the fact that theoretical contact angle values derived from either the Cassie or the Wenzel equation often are in good agreement with experimentally determined contact angles, this is not always the case. For example, Extrand[33] showed that the contact angle measured for a

(17) Wang, J.; Hu, J.; Wen, Y.; Song, Y.; Jiang, L. *Chem. Mater.* **2006**, *18*, 4984.
(18) Han, J. T.; Zheng, Y.; Cho, J. H.; Xu, X.; Cho, K. *J. Phys. Chem. B* **2005**, *109*, 20773.
(19) Chen, X. D.; Hirtz, M.; Fuchs, H.; Chi, L. F. *Adv. Mater.* **2005**, *17*, 2881.
(20) Wang, C.-W.; Moffitt, M. G. *Chem. Mater.* **2005**, *17*, 3871.
(21) Yu, X.; Wang, Z.; Jiang, Y.; Zhang, X. *Langmuir* **2006**, *22*, 4483.
(22) Parikh, A. N.; Allara, D. L.; Azouz, I. B.; Rondelez, F. *J. Phys. Chem.* **1994**, *98*, 7577.
(23) Haidara, H.; Mougin, K.; Castelein, G.; Schultz, J. *Langmuir* **2000**, *16*, 9121.
(24) Xu, S.; Miller, S.; Laibinis, P. E.; Liu, G.-Y. *Langmuir* **1999**, *15*, 7244.
(25) Lim, J. Y.; Hansen, J. C.; Siedlecki, C. A.; Hengstebeck, R. W.; Cheng, J.; Winograd, N.; Donahue, H. J. *Biomacromolecules* **2005**, *6*, 3319.
(26) Meli, M.-V.; Lennox, R. B. *Langmuir* **2007**, *23*, 1619.
(27) Fisher, A.; Kuemmel, M.; Järn, M.; Lindén, M.; Boissière, C.; Nicole, L.; Sanchez, C.; Grosso, D. *Small* **2006**, *2*, 569.
(28) Wenzel, R. N. *Ind. Eng. Chem.* **1936**, *28*, 988.
(29) Cassie, A. B. D. *Discuss. Faraday Soc.* **1948**, *3*, 11.
(30) Cassie, A. B. D.; Baxter, S. *Trans. Faraday Soc.* **1944**, *40*, 546.
(31) He, B.; Patankar, N. A.; Lee, J. *Langmuir* **2003**, *19*, 4999.
(32) Patankar, N. A. *Langmuir* **2004**, *20*, 7097.
(33) Extrand, C. W. *Langmuir* **2003**, *19*, 3793.

heterogeneous surface cannot be described using the Cassie formalism when the size of the droplet is comparable to the length scale of the heterogeneity of the surface and that the energy balance at the three-phase contact line is the decisive parameter. Support for this view was also presented in another recent study by Gao and McCarthy,[34] and they suggested that the Wenzel and Cassie equations are valid only to the extent that the structure of the contact area reflects the ground-state energies of contact lines and the transition states between them. In a very recent study, McHale[35] emphasized that the original Cassie surface fraction and Wenzel roughness parameter should be viewed as global properties of the surface rather than properties of the contact area below the droplet. Nosonovsky[36] used a surface-energy approach to show that the original Wenzel and Cassie equations are valid only for uniformly rough surfaces. Generalized Wenzel and Cassie equations should be applied for nonuniformly rough surfaces. Another criterion for the validity of the Wenzel and Cassie equations is that the scale of the roughness/heterogeneity must be small compared to the length of the three-phase contact line.[37,38] Similar conclusions were derived from theoretical calculations.[39]

For hydrophilic films, capillary effects have also been suggested to be important for the creation of superhydrophilic surfaces. For metal oxide semiconductors with surface photosensitivity, selective molecular adsorption on activated surface sites has been suggested to result in the formation of surface hydrophilic domains and leave the rest of the surface area oleophilic.[40] High-resolution friction force microscopy (FFM) analysis has suggested that oleophilic areas are positioned lower than hydrophilic domains, indicating that oleophilic and hydrophilic walls might form channels for water and oil flow, respectively, in a manner similar to a 2D capillary phenomenon. Furthermore, a 3D capillary phenomenon has been suggested by Bico and co-workers[41,42] to account for the observation of hydrophilicity on one-component surfaces in the Wenzel state.

Also, contact-angle hysteresis, i.e., the difference between the advancing and receding contact angles, is an important factor in describing the wettability of a surface. A small hysteresis or a small roll-off angle is essential for a surface to be called hydrophobic.[43,44] Often only static or advancing contact angles are reported, giving an incomplete description of the wetting properties of a surface.

In the following, we report results related to the wetting properties of nanoperforated TiO_2 layers deposited on SiO_2 or Au and of selectively hydrophobically functionalized films. The results can be theoretically modeled, as all important parameters needed for a theoretical evaluation of the wetting characteristics of the films can be accessed experimentally. On the basis of experimentally determined parameters, we show that the wetting of these model surfaces can be described as Cassie−Baxter, Cassie−Wenzel, or capillary wetting, depending on the hydrophilic−hydrophobic contrast of the films and hydrodynamic effects.

Experimental Procedures

A detailed description of the synthesis of the films and the functionalization of titania with the Zonyl function $(CF_3(CF_2)_2(CH_2)_5O)_2POO^-$ has been published elsewhere.[27,45] Briefly, initial sols were prepared by dissolving $TiCl_4$ and EO_n-*b*-[(E)B]$_m$ [poly(ethylene oxide)-*block*-poly(ethylene-*co*-butylene), e.g., $H(CH_2CH_2CH_2CH(CH_3)CH_2)_{320}$-*b*-$(OCH_2CH_2)_{568}H$ synthesized at the Max Planck Institute of Colloids and Interface, Golm, Germany] in mixtures of ethanol, water, and/or THF. To obtain large craters, the following mixture was used: 1 g of $TiCl_4$, 1.5 g of EO-*b*-[(E)B], 65 g of EtOH, and 1.1 g of H_2O. Small craters were obtained when 35 g of THF was included in the mixture, as a result of increased copolymer solubility. The solutions were heated to 70 °C and then allowed to cool slowly to room temperature in order to ensure homogeneous micellization. The solutions were then deposited on silicon wafers ([111], B-doped, coated with a native 2.5 nm thick layer of SiO_2) or on gold-deposited wafers by dip coating at a constant withdrawal rate of 1.5 mm s^{-1} with a fixed relative humidity of 30% at room temperature, using a KSV DipCoater DC (KSV Instruments Ltd., Helsinki, Finland). The films were dried for 5 min, transferred onto a heating plate, and calcined at 500 °C for 3 min. Functionalization was accomplished by immersing the films into a 1 wt % aqueous solution of Zonyl for 30 min. These functionalized films are labeled "TO".

AFM images were recorded using a Nanoscope IIIa atomic force microscope (Digital Instruments, Santa Barbara, CA). All of the images were recorded in tapping mode using silicon cantilevers with a resonance frequency between 250 and 300 kHz. The scan rate was typically 1 Hz. The free tapping amplitude was 70–100 nm for the high-kinetic-energy tapping measurements. The damping ratio r_{sp} (= A_{sp}/A_0) controlling the level of forced damping was chosen by tuning the set-point amplitude A_{sp}. All images (512 × 512 pixels) were measured in air without filtering. The microscope was placed on an active vibration isolation table (MOD-1M, JRS Scientific Instruments, Zwillikon, Switzerland), which in turn was placed on a massive stone table to eliminate external vibrational noise. Scanning Probe Image Processor (SPIP) software (Image Metrology, Hørsholm, Denmark) was used for image analysis.[46] Images of the films were also taken using a scanning electron microscope (JSM-6335F, JEOL Ltd., Tokyo, Japan). These samples were coated with platinum prior to analysis.

The thickness of the surface layer was measured in dry air at ambient temperature using variable angle spectroscopic ellipsometry (VASE, Woolam 2000U) at incidence angles of 65, 70, and 75° in the spectral range 400−1000 nm. The Bruggeman effective-medium approximation was used to take into account the volume fraction of air associated with the craters.

Cyclic voltametry curves were measured using a Solartron apparatus. The redox probe was $Fe(CN)_6^{3-}/Fe(CN)_6^{4-}$ diluted to 5 mM in an aqueous solution containing 0.1 M KCl. The scan rate was 50 mV s^{-1}. The measurement was performed at 25 °C under

(34) Gao, L.; McCarthy, T. J. *Langmuir* **2007**, *23*, 3762.
(35) McHale, G. *Langmuir* **2007**, *23*, 8200.
(36) Nosonovsky, M. *Langmuir* **2007**, *23*, 9919.
(37) Barbieri, L.; Wagner, E.; Hoffmann, P. *Langmuir* **2007**, *23*, 1723.
(38) Nosonovsky, M. *Langmuir* **2007**, *23*, 3157.
(39) Iliev, S. D.; Pesheva, N. C. *Langmuir* **2003**, *19*, 9923.
(40) Wang, R.; Sakai, N.; Fujishima, A.; Watanabe, T.; Hashimoto, K. *J. Phys. Chem. B* **1999**, *103*, 2188.
(41) Bico, J.; Tordeux, C.; Quéré, D. *Europhys. Lett.* **2001**, *55*, 114.
(42) Bico, J.; Tordeux, C.; Quéré, D. *Colloids Surf., A* **2002**, *206*, 41.
(43) Chen, W.; Fadeev, A. F.; Hsieh, M. C.; Öner, D.; Youngblood, J.; McCarthy, T. J. *Langmuir* **1999**, *15*, 3395.
(44) Yoshimitsu, Z.; Nakajima, A.; Watanabe, T.; Hashimoto, K. *Langmuir* **2002**, *18*, 5818.
(45) Kuemmel, M.; Allouche, J.; Nicole, L.; Boissière, C.; Laberty, C.; Amenitsch, H.; Sanchez, C.; Grosso, D. *Chem. Mater.* **2007**, *19*, 3717.
(46) Image Metrology A/S. *The Scanning Probe Image Processor, SPIP, User's and Reference Guide*; Copenhagen, 2001.

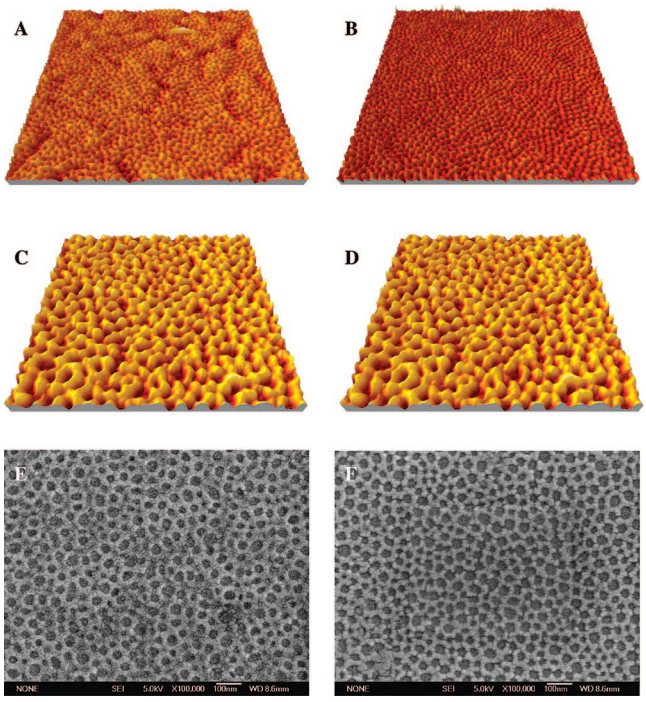

Figure 1. AFM images and SEM micrographs of small- and large-crater TiO_2 films on gold and silica substrates: (A) 1 μm × 1 μm AFM image of a small-crater TiO_2 film on gold (Z range = 16.4 nm); (B) 1 μm × 1 μm AFM image of a small-crater TiO_2 film on silica (Z range = 13.6 nm); (C) 1 μm × 1 μm AFM image of a large-crater TiO_2 film on gold (Z range = 26.6 nm); (D) 1 μm × 1 μm AFM image of a large-crater TiO_2 film on silica (Z range = 18.8 nm); (E) SEM micrograph of a large-crater TiO_2 film on gold; (F) SEM micrograph of a large-crater TiO_2 film on silica.

continuous stirring after bubbling with N_2 for 30 min to remove O_2 from the solution, using a constant electrode surface area of 0.4 cm^2. Since TiO_2 is a semiconductor, we selected a hexacyanoferrate probe because its oxidation and reduction, both of which occur at potentials greater than 0 V, are well-separated from the reduction of Ti(IV), which occurs at a potential less than −0.2 V. The signal can thus be safely ascribed to reaction between the probe and the accessible gold surface.

A CAM 200 contact angle goniometer (KSV Instruments Ltd.) was used for determination of water contact angles. The contact angles were calculated using the software supplied with the instrument. Typically, a 2 μL droplet was deposited on the surface, and the static contact angle θ_{stat} was determined. Then water was slowly added in order to determine the advancing contact angle θ_{adv}. Subsequently, liquid was removed from these droplets in order to determine the receding contact angle θ_{rec}. Static contact angles were also determined for droplets of larger volume (~6.5 μL), which were dropped onto the surface from a specified distance. The results given are mean values of 3–5 measurements, with a standard deviation of less than 3° for the composite films. The standard deviations of the contact angles measured for the one-component reference surfaces are given in Table 2.

Results and Discussion

Initially, a detailed structural evaluation of the nanoperforated layers was performed in order to define all of the parameters necessary for a correct estimation of the critical parameters needed for evaluating the contact angle data. In Figure 1, AFM images and SEM pictures of TiO_2/Au and TiO_2/SiO_2 composite surfaces with small (11 nm mean diameter) and large (30 nm mean diameter) craters are

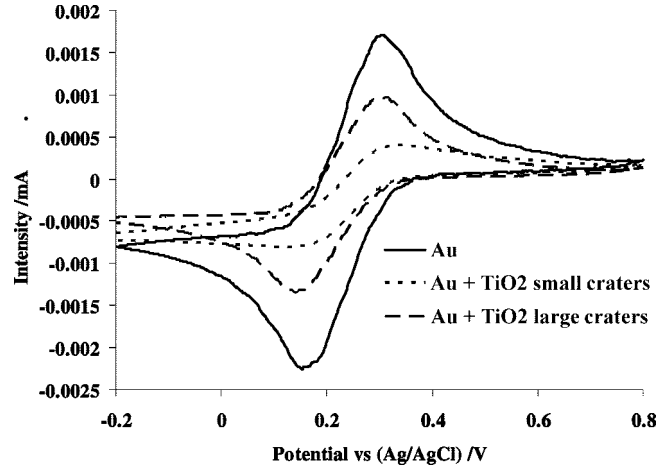

Figure 2. Cyclic voltammetry curves measured for a bare Au electrode (solid curve), a TiO_2/Au surface with small craters (dotted curve), and a TiO_2/Au surface with large craters (dashed curve).

shown. For the small-crater layers, one can clearly see a nice ordering of the craters with a narrow distribution of crater sizes and a homogeneous crater-wall thickness. The crater-size distribution was wider for the large-crater layers, but the layers were homogeneous and had an even thickness in this case also. The mean wall thickness was 10 nm for the small-crater films, 15 nm for the large-crater TiO_2/SiO_2 surfaces, and 18 nm for the large-crater TiO_2/Au surfaces. The mean crater sizes and the crater-size distributions were very similar regardless of whether gold or silica constituted the substrate. The film thicknesses were determined by ellipsometry and generally were in good agreement with those obtained from the AFM measurements. The small-crater films had a thickness of 5.5 nm, while the large-crater film thickness was 11 nm.

The accessible fraction of the substrate area measured for macroscopic dimensions could be estimated by electrochemical means for the TiO_2/Au films, as the Au substrate is electrically conducting. Figure 2 shows cyclic voltammetry curves corresponding to a bare electrode (Au) and nanoperforated TiO_2-modified Au electrodes (TiO_2/Au with large and small craters). The signals were characteristic of quasi-reversible systems with overpotentials ($\Delta V = 0.16$, 0.17, and 0.23 V for the Au, large-crater TiO_2/Au, and small-crater TiO_2/Au electrodes, respectively). The Faradic peak currents obtained after subtraction of the residual capacitive currents were $I^{ox} = 1.71$ μA and $I^{red} = 1.69$ μA for Au, $I^{ox} = 0.37$ μA and $I^{red} = 0.36$ μA for TiO_2/Au composite layers with small craters, and $I^{ox} = 0.96$ μA and $I^{red} = 0.94$ μA for TiO_2/Au large-crater composite layers. The nanocrater-modified electrodes still exhibited high peak-current intensities, but these intensities were smaller than that of the bare Au electrode in the reduction and oxidation modes. The very slight increase of the corresponding overpotentials compared with that of the bare electrode indicated that no reduction of mass and charge transfers could be attributed to the nanoperforated layer, suggesting that the perforation does not introduce any diffusion barrier. The slight sigmoidal shape of the TiO_2-modified electrodes with small craters was associated with a slight radial contribution of the diffusion regime, which was consistent with such a nanoelectrode array

Table 1. Measured Mean Crater Diameter (D), Wall Thickness (w), and Surface-Layer Thickness (h) Values and Calculated Wenzel Parameter (r) and Cassie−Baxter (f_{TiO_2}) and Cassie−Wenzel (F_{TiO_2}) TiO_2 Fractional Area Values for the Nanoperforated Composite Layers

					f_{TiO_2}		F_{TiO_2}	
sample	D (nm)[a]	w (nm)[a]	h (nm)[b]	r[c]	structural[d]	cycl. volt.[e]	structural[f]	cycl. volt.[e]
TiO_2/Au with small craters	11 ± 2	10 ± 2	5.5	1.66	0.75	0.78	0.83	0.85
TiO_2/Au with large craters	31 ± 7	18 ± 3	11	1.79	0.65	0.44	0.76	0.58
TiO_2/SiO_2 with small craters	11 ± 2	10 ± 1	5.5	1.66	0.75	−	0.83	−
TiO_2/SiO_2 with large craters	29 ± 7	15 ± 1	11	1.96	0.63	−	0.76	−

[a] Obtained from AFM and SEM images. [b] Measured using ellipsometry. [c] Calculated according to eq 12. [d] Calculated from AFM and SEM data according to eq 11. [e] Determined from cyclic voltammetry measurements. [f] Calculated according to eq 4.

Table 2. Measured Contact Angles (Static, Advancing, and Receding) for the Reference Surfaces

reference	θ_{stat} (deg)	θ_{adv} (deg)	θ_{rec} (deg)
TiO_2	<5	<5	0
SiO_2	7 ± 3	10 ± 2	0
Au	80 ± 4	88 ± 1	42 ± 3
TO-TiO_2	88 ± 4	100 ± 1	60 ± 2
TO-SiO_2	25 ± 1	28 ± 1	0
TO-Au	69 ± 2	81 ± 1	37 ± 4

morphology.[47] In this case, the maximal peak current intensity could be directly associated with the fraction of Au substrate in contact with the solution. Since the macroscopic surface area of the electrodes was kept constant (0.4 cm^2) in all measurements, the fractional area of the accessible Au substrate could be estimated by comparing the intensities recorded with the bare electrode and the modified electrodes. The fractions of accessible surface area of the Au substrate determined in this way for the small- and large-crater TiO_2/Au layers were 0.22 and 0.56, respectively, using mean values for I^{ox} and I^{red} (see Table 1). We also estimated the corresponding fractional areas from the SEM and AFM images, which probe the local structure of the surface, and these results are also given in Table 1. For the small-crater layers, the value of 0.25 for the (2D) fraction of accessible surface area obtained from the structural methods was very similar to that obtained using cyclic voltammetry (0.22), while for the large-crater layers, the structural value of 0.35 differed quite substantially from the electrochemical value (0.56). The larger area of accessible substrate measured by the electrochemical characterization can partly be explained by the presence of microcracks in the TiO_2 network that were observed by SEM but not taken into account in the fractional-area determination based on the AFM and SEM results. In any case, as discussed above, it is clear that the small-crater layers were more structurally homogeneous than the large-crater layers.

As discussed in the Introduction, the value of the r parameter in the Wenzel equation (eq 1) must be known in order to model the wetting behavior of surface-functionalized films. The value of r is important for the TiO_2 portion of the surface layer in order to account for the additional surface area introduced by surface roughness, which thus leads to modified values of f_1 and f_2 in the Cassie equation (eq 2). For the fractional areas of the substrates (f_{Au} and f_{SiO_2}), we used the values obtained from the electrochemical analysis, as a bulk analysis rather than a microanalysis better corresponds to the surface experienced by the deposited water droplet. The r value was calculated from crater diameter values obtained using AFM and SEM and the surface-layer thickness value obtained using ellipsometry. Because the Wenzel approach is valid only for homogeneous surfaces and the Cassie approach is valid only for smooth surfaces, we first needed to combine these equations in order to correctly describe the present films. For the fully wetting Wenzel case, the additional surface area of the TiO_2 portion of the surfaces modifies the fractions f_1 and f_2 in eq 2 (assuming that the Au or SiO_2 fraction is flat). These modified values, here denoted F_1 and F_2, also must fulfill the criterion $F_1 + F_2 = 1$. The corrected equation that accounts for surface roughness can then be written as follows:

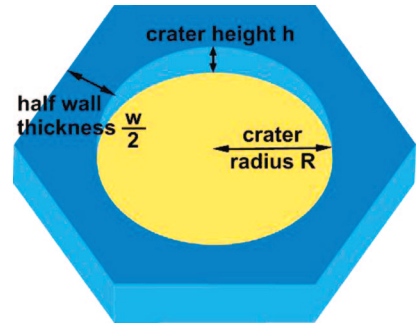

Figure 3. Schematic representation of one unit cell of the nanoperforated layer.

$$\cos\theta_A = F_1 \cos\theta_1 + F_2 \cos\theta_2 \quad (4)$$

where the modified surface fractions are given by the formulas

$$F_1 = \frac{rf_1}{rf_1 + f_2} \quad \text{and} \quad F_2 = \frac{f_2}{rf_1 + f_2}$$

We call eq 4 the Cassie−Wenzel equation. Combinations of the Cassie−Baxter and Wenzel equations have also been used previously to describe the wetting of rough surfaces on different length scales.[48] In the discussion below, the symbol f_1 (or F_1) refers to the TiO_2 (or TO-TiO_2) fraction of the layers. In order to determine an r value, we approximated one unit cell of the nanoperforated layer as shown in Figure 3.

The projected area A_{2D} of the unit-cell hexagon is given by

$$A_{2D} = 2\sqrt{3}\left(R + \frac{w}{2}\right)^2 \quad (5)$$

where $R$is the crater radius and w is the thickness of the wall separating adjacent craters. The area A_{wall} of the

(47) Valsesia, A.; Lisboa, P.; Colpo, P.; Rossi, F. *Anal. Chem.* **2006**, *78*, 7588.

(48) Shirtcliffe, N. J.; McHale, G.; Newton, M. I.; Perry, C. C. *Langmuir* **2005**, *21*, 937.

cylindrical wall of the crater, which depends on the crater height h (i.e., on the surface layer thickness), is

$$A_{\text{wall}} = 2\pi Rh \tag{6}$$

Adding these two contributions yields A_{3D}, the total 3D surface area of the unit cell:

$$A_{3D} = 2\sqrt{3}\left(R + \frac{w}{2}\right)^2 + 2\pi Rh \tag{7}$$

The accessible area of the substrate (Au or SiO_2) in the unit cell is given by

$$A_{\text{substrate}} = \pi R^2 \tag{8}$$

Subtracting eq 8 from eq 7 gives an overall expression for the accessible 3D titania surface area A_{TiO_2}–3D:

$$A_{TiO_2-3D} = A_{3D} - A_{\text{substrate}} = 2\sqrt{3}\left(R + \frac{w}{2}\right)^2 + 2\pi Rh - \pi R^2 \tag{9}$$

Taking into account only the projected unit-cell area (i.e., neglecting the crater-wall area) gives the accessible 2D titania surface area A_{TiO_2}–2D:

$$A_{TiO_2-2D} = 2\sqrt{3}\left(R + \frac{w}{2}\right)^2 - \pi R^2 \tag{10}$$

The projected-area fraction of titania, f_{TiO_2}, is then given by

$$f_{TiO_2} = \frac{A_{TiO_2-2D}}{A_{2D}} \tag{11}$$

Finally, the value of r is given by

$$r = \frac{A_{TiO_2-3D}}{A_{TiO_2-2D}} \tag{12}$$

Since the crater-size distribution is rather broad for the large-crater layers, the calculated r value is a weighted average of the contributions from the various crater sizes. However, simply using the mean crater size as the input diameter gave an almost identical value of r. The 3D F values given in Table 1 were determined using r values obtained from structural analysis and f_1 and f_2 values obtained from either structural or electrochemical analysis.

The water contact angles were first determined on one-component and TO-functionalized TiO_2, SiO_2, and gold reference surfaces. The results are presented in Table 2. As expected, the flat TiO_2 and SiO_2 surfaces were very hydrophilic, while the Au reference surface was slightly hydrophilic, with a static contact angle $\theta_{\text{stat,Au}}$ of 80°. Exact values of the contact angles for the hydrophilic TiO_2 and SiO_2 reference surfaces were difficult to determine because of the nearly full spreading of the droplet, but the errors introduced by this difficulty were negligible since the cosine of the contact angle is used in the model calculations,. Only the TiO_2 surface became clearly more hydrophobic ($\theta_{\text{stat,TO-TiO}_2} = 88°$, $\theta_{\text{adv,TO-TiO}_2} = 100°$) upon Zonyl functionalization, in agreement with previous reports.[27] The probable reason for the difference in the water contact angles of the untreated and Zonyl-treated silica and Au surfaces is the different pretreatments applied before the measurements. In the case of the untreated surface, the contact angle was measured directly after heat treatment of the silica surface, while in the case of Zonyl-functionalized films, the samples were simply rinsed with water and ethanol and dried in a stream of air before the measurement, in order to avoid decomposing the surface function.

The contact angles measured for the nanopatterned surfaces are summarized in Table 3. Note that full wetting was observed for both the TiO_2/Au and TiO_2/SiO_2 films, even though the pure Au reference showed a fairly large contact angle ($\theta_{\text{stat,Au}} = 80°$) and the fraction of Au in the composite films was 20–50%.

The Zonyl-functionalized hybrid films all showed static and advancing contact angles of >100° for 2 μL droplets, i.e., they were all hydrophobic and had larger contact angles than either of their constituents. The large-crater surfaces generally showed larger contact angles than the small-crater surfaces, with advancing contact angles of 112 and 116° for small-crater and 127 and 128° for large-crater TO-TiO_2/Au and TO-TiO_2/SiO_2 surfaces, respectively. The receding contact angles were significantly smaller for all of the surfaces, ranging from ~15 to ~50°.

Given the respective f_1, f_2, F_1, and F_2 values, theoretical contact angles were calculated for the nonfunctionalized or Zonyl-functionalized nanopatterned TiO_2 surfaces according to the Cassie−Baxter and Cassie−Wenzel equations. These values are given in Table 3. Here, the contact angles measured for the reference surfaces that had undergone similar pretreatments as the nanopatterned films were used (see Table 2). The standard deviations for the theoretically calculated contact angles were at most 4° and in most cases less than 2°. The observed complete wetting of the bare TiO_2/Au and TiO_2/SiO_2 nanoperforated layers could not be ascribed to either Cassie(−Baxter)- or Wenzel-type wetting and clearly originated from 3D capillary wetting induced by

Table 3. Experimental Water Contact Angles Determined Using 2 μL Water Droplets and Theoretical Contact Angles Predicted Using the Cassie−Baxter and Cassie−Wenzel Models for the Composite Surfaces

				Cassie−Baxter prediction (deg)						Cassie−Wenzel prediction (deg)					
	experimental contact angle (deg)			structural			cycl. volt.			structural			cycl. volt.		
sample	θ_{stat}	θ_{adv}	θ_{rec}	θ_{stat}	θ_{adv}	θ_{rec}	θ_{stat}	θ_{adv}	θ_{rec}	θ_{stat}	θ_{adv}	θ_{rec}	θ_{stat}	θ_{adv}	θ_{rec}
TiO_2/Au with small craters		full wetting		60	60	60	56	56	56	31	34	17	29	32	16
TiO_2/Au with large craters		full wetting		73	73	73	97	97	97	37	40	20	49	54	27
TiO_2/SiO_2 with small craters		full wetting		60	60	60	56	56	56	5	6	0	5	6	0
TiO_2/SiO_2 with large craters		full wetting		75	75	75	97	97	97	6	7	0	6	7	0
TO-TiO_2/Au with small craters	103	112	44	103	112	83	101	111	80	85	97	57	85	97	57
TO-TiO_2/Au with large craters	119	127	23	109	118	91	123	130	110	84	95	55	80	92	51
TO-TiO_2/SiO_2 with small craters	107	116	47	103	112	83	101	111	80	79	90	54	80	91	55
TO-TiO_2/SiO_2 with large craters	121	128	13	110	119	93	123	130	110	76	85	52	68	76	46

the presence of hydrophilic nanocraters.[41,42] The craters would have been filled with liquid due to capillary effects, causing the contact line to advance along the superhydrophilic TiO_2 network, ultimately leading to complete wetting.

For the small droplets on Zonyl-functionalized composite surfaces, the measured static and advancing water contact angles were modeled with high accuracy using the Cassie−Baxter theory. Thus, despite the use of very thin films (5.5 and 11 nm small- and large-crater film thicknesses, respectively), air is assumed to be trapped in the craters, resulting in a solid−air composite surface, although the Laplace pressure would have been very high for air bubbles with diameters of only 10–30 nm. However, the occurrence of trapped air bubbles is in agreement with recent molecular dynamics studies.[49] The lifetime of such small gas bubbles in water has been suggested to be in the range of only 1 μs, with the internal pressure of the bubble estimated using the Laplace equation.[50,51] It has also been suggested that the number of gas molecules in a nanosized bubble may be small, which would lead to an internal pressure lower than that suggested by the Young-Laplace equation and thus to increased nanobubble stability.[52] Nanobubbles in this size range have also been reported on the basis of AFM measurements on hydrophobic smooth surfaces.[53] Furthermore, it has been suggested that line-tension effects may flatten air bubbles at the interface, thus stabilizing the bubbles;[54] this effect has also been observed experimentally.[55] We note, however, that chemically uniform surfaces were considered in all of those cases and that the nanopatterned surfaces under study in the present work may introduce yet another mode of nanobubble stabilization that is based on geometrical as well as surface-energy-inhomogeneity effects, which may increase the nanobubble lifetime on the surface to several tens of minutes, as observed here. Evaporation effects make it difficult to correctly estimate the contact angles on time scales of hours.

The receding contact angles could not be modeled accurately using the Cassie−Baxter theory. Instead, the Cassie−Wenzel model fit the results better, though some divergence was still present. This raises doubts about whether air was actually located in the craters below the static and advancing droplets. However, Nosonovsky et al.[56] recently reported that contact-angle hysteresis cannot be determined from macroscale equations and should rather be seen as a micro- or nanoscale phenomenon. Several authors have reported on the difference in hysteresis between Cassie−Baxter and Wenzel droplets.[57,58] The Cassie−Baxter state is often called a "slippery" state, in which the hysteresis is small and a droplet easily rolls off the surface. On the contrary, the Wenzel state, in which the hysteresis is large, is called a "sticky" state. However, Shirtcliffe et al.[58] studied rough, electrodeposited copper-based samples with very large static water contact angles, which did not follow Wenzel behavior. The contact-angle hysteresis was significant, even though a considerable amount of the surface was bridged by the water droplet, i.e., a Cassie−Baxter-type state was present. This finding suggests that contact-angle hysteresis cannot entirely describe the type of wetting present. McCarthy et al.[43] stressed the influence of the shape and length of the three-phase contact line on contact-angle hysteresis. In other words, the geometry of the surface plays an import role in the hysteresis behavior. For example, on a surface consisting of separated posts, a short, discontinuous contact line can form, causing no pinning when the contact line is moved. Subsequently, the hysteresis is very small. For our surfaces, on the other hand, a fairly long, continuous contact line can form on the continuous TiO_2 network, pinning the droplet when liquid is added or removed. The energy that is required to jump over the contact line from one metastable state to another is quite large, and the hysteresis is therefore large as well. Dorrer and Rühe[59] showed that the receding motion of the contact line is a complicated process and that the geometry of the surface strongly affects the receding angle. Identical solid fractions having different surface geometries (post distances and sizes) gave rise to large variations in the receding angle. The measured receding angles of the large-crater samples deviated from the modeled results to a greater extent than the small-crater samples, possibly as a result of the difference in geometry. The large hysteresis observed here could also be due to a possible intermediate state between the Cassie−Baxter and Cassie−Wenzel modes.[6] Extrand[60] presented a contact-line density model for rough and hydrophobic surfaces that accounts for contributions from sharp edges of the surface when determining the advancing and receding contact angles. However, determining the fractional contributions of the contact line on our nanopatterned surfaces was not trivial with this model, since the contact line probably was heavily distorted.[61] However, our use of the Cassie and Wenzel models in this study should be valid, since the roughness and heterogeneity of our nanopatterned surfaces were uniform.[35,36] Additionally, the scale of the roughness/heterogeneity was small compared to the length of the three-phase contact line.[37–39]

To further investigate the wetting characteristics of our nanopatterned surfaces, larger droplets ($\sim$6.5 μL) were dropped from some height onto the Zonyl-functionalized nanopatterned layers. The static contact angles measured for both small- and large-crater nanoperforated layers ($<90°$) were significantly smaller than those for the gently deposited smaller droplets. As an example, snapshots measured for small-crater TO-TiO_2/Au surfaces are shown in Figure 4. This case thus seems to represent a transition from a Cassie−Baxter state to a Cassie−Wenzel state, suggesting that the craters became filled with liquid when a larger

(49) Lundgren, M.; Allan, N. L.; Cosgrove, T. *Langmuir* **2007**, *23*, 1187.
(50) Ljunggren, S.; Eriksson, J. C. *Colloids Surf., A* **1997**, *129–130*, 151.
(51) Epstein, P. S.; Plesset, M. S. *J. Chem. Phys.* **1950**, *18*, 1505.
(52) Nagayama, G.; Tsuruta, T.; Cheng, P. *Int. J. Heat Mass Transfer* **2006**, *49*, 4437.
(53) Ishida, N.; Inoue, T.; Miyahara, M.; Higashitani, K. *Langmuir* **2000**, *16*, 6377.
(54) Boehnke, U.-C.; Remmler, T.; Motschmann, H.; Wurlitzer, S.; Hauwede, J.; Fischer, T. M. *J. Colloid Interface Sci.* **1999**, *211*, 243.
(55) Yang, J.; Duan, J.; Fornasiero, D.; Ralston, J. *J. Phys. Chem. B* **2003**, *107*, 6139.
(56) Nosonovsky, M.; Bhushan, B. *Nano Lett.* **2007**, *7*, 2633.
(57) He, B.; Lee, J.; Patankar, N. A. *Colloids Surf., A* **2004**, *248*, 101.
(58) Shirtcliffe, N. J.; McHale, G.; Newton, M. I.; Perry, C. C. *Langmuir* **2005**, *21*, 937.
(59) Dorrer, C.; Rühe, J. *Langmuir* **2006**, *22*, 7652.
(60) Extrand, C. W. *Langmuir* **2002**, *18*, 7991.
(61) Dorrer, C.; Rühe, J. *Langmuir* **2007**, *23*, 3179.

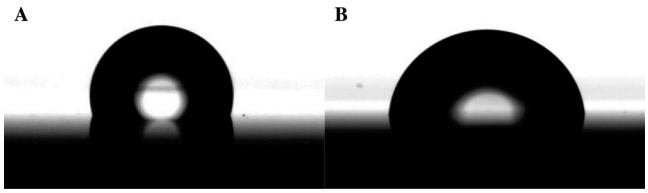

Figure 4. Water droplets on TO-TiO_2/Au films with small craters: (A) gently deposited small water droplet (drop volume $\approx$ 2 μL, θ_{stat} = 103°); (B) large droplet dropped from some height (drop volume $\approx$ 6.5 μL, θ_{stat} = 85°).

droplet was dropped onto the surface. Similar tests were also done on smooth TiO_2 and Au reference surfaces, and no differences in contact angle compared with the results for the gently deposited droplets were observed. For these larger droplets, the static contact angles of the Zonyl-functionalized composites were better described by the Cassie−Wenzel theory, suggesting that the energy barrier between the Cassie−Baxter and Cassie−Wenzel states was low. This activation energy could be overcome by dropping a larger droplet from some height, in agreement with both experimental observations[31,32] and theoretical predictions.[62] Very interestingly, however, when more liquid was added to the larger droplet, the advancing contact angle increased to values similar to those for the smaller droplets. This result, together with the receding contact angle data, provides some indication that the craters could have been filled with liquid below the droplet and that the three-phase contact line was the decisive factor in determining the contact angle. The good agreement between the experimentally determined contact angle values and those derived using either the Cassie or the Wenzel equation would in that case be related to the fact that the area fractions accurately describe the surface composition along the three-phase contact line for these nanopatterned films.

Thus, depending on the hydrophilicity of the mesoporous TiO_2 network (Zonyl-functionalized or not) and the method of water-droplet deposition, three different wetting behaviors were identified. Superhydrophilicity assigned to 3D capillary wetting was observed on nonfunctionalized nanopatterned surfaces. However, we note that both components of the TiO_2/SiO_2 film were very hydrophilic, making it difficult to distinguish between capillary wetting and Cassie−Wenzel-type wetting in this case. For gently deposited small water droplets on Zonyl-functionalized nanopatterned surfaces, the measured contact angles were higher than those for either of its constituents. These results could be modeled using the Cassie−Baxter equation, which assumes that air is entrapped in the craters. The contact angles decreased significantly when larger water droplets were dropped from some height onto the same surfaces. These contact angles fit better to Cassie−Wenzel-type wetting. The large contact-angle hysteresis on the Zonyl-functionalized nanopatterned layers possibly could have been caused by the geometry of the surface, since a fairly long continuous contact line was able to take shape as a result of the continuity of the TiO_2 network. The large hysteresis observed here could possibly be decreased using a different geometry for the TiO_2 layer, such as separated nanodots of TiO_2. The shift from Cassie−Baxter- to Cassie−Wenzel-type wetting when a larger droplet was dropped, together with the large contact-angle hysteresis, suggests the possibility that an intermediate state between the Cassie−Baxter and Cassie−Wenzel modes exists. Also, the return to Cassie−Baxter-type wetting when liquid was added to the large droplet suggests that interactions at the three-phase contact line determine the wetting. This result then also implies that, at least close to the three-phase contact line, nanobubbles are stable on time scales of several minutes, although the existence of these bubbles was very difficult to verify experimentally for the films under study.

Conclusion

We have observed very different wetting behaviors for the various heterogeneous nanopatterned surfaces studied, and the wetting behavior depended on the structure, the surface functionalization, and the method of depositing the droplet onto the surface. Detailed structural characterization of the nanoperforated layers using AFM, SEM, ellipsometry, and electrochemistry allowed the results to be quantitatively evaluated on the basis of existing models for wetting of heterogeneous and rough surfaces. Very few if any detailed wetting studies have previously been done on materials with heterogeneities of this length scale. Since different morphological structures are quite easily achievable through the EISA technique,[45] further wetting studies of such nanostructured materials would be of great interest in fields such as sensing and microelectronics.

Acknowledgment. We thank Mr. Niklas Björklund for preparing some of the Au substrates. M.J. and F.J.B. gratefully acknowledge the Finnish Academy for financial support.

CM702870R

(62) Werner, O.; Wågberg, L.; Lindström, T. *Langmuir* **2005**, *21*, 12235.